Improvement of the cloud top height algorithm for the fundamental cloud product and related evaluation

MOURI Kouki*

Abstract

Himawari-8/AHI was put into active operation in July 2015 in association with JMA/MSC's utilization of a cloud top height estimation algorithm following conventional methods such as the infrared window, IR-WV intercept and radiance ratioing techniques. In verification based on satellite-borne lidar analysis, the correlation coefficient of the JMA/MSC cloud top height was approximately 0.75 in relation to the cloud top product based on satellite-borne lidar. In other work, NOAA also developed a new cloud top height estimation algorithm for the GOES-R/ABI imager, which is very similar to Himawari-8/AHI (except for the 0.51 and 1.3 μm bands), particularly in terms of their infrared bands and therefore it was considered to be easy to incorporate the algorithm to Himawari-8/AHI. JMA/MSC tested the GOES-R cloud top height estimation algorithm based on its new concept, and partially expanded the cloud radiative model used in the algorithm to deal with two-layer cloud situations. As a result of the modification, the mean error (which indicates the systematic error) and the correlation coefficient was improved. This report outlines the cloud top height algorithm and its expansion to the two-layer cloud model, and also briefly describes the cloud type and cloud phase product produced with the GOES-R algorithm as a mandatory element in cloud top height estimation.

1. Introduction

The Japan Meteorological Agency's Meteorological Satellite Center (JMA/MSC) began providing a cloud top height estimation product (Mouri et al. 2016) at the beginning of Himawari-8's service period (Bessho et al. 2016) in July 2015. The related algorithm combined the infrared window technique (Nieman et al. 1993), the radiance ratioing technique (Menzel et al. 1983) and the IR-WV intercept technique (Schmetz et al. 1993), which have also been used in cloud top height estimation algorithms by various countries. JMA/MSC initially tested this time-proven algorithm approach using data from Europe's geostationary Meteosat Second-Generation meteorological satellite (Schmetz et al. 2002), which has 12 observation wavelength bands, and adopted the method for operational cloud top height estimation with Himawari-8. In February 2017, the correlation coefficient indicating the accuracy of the cloud top height estimation product was 0.75 and the mean error indicating systematic error was -903 m. The reference information was layer top altitude data recorded in the Level 2 Cloud-Aerosol Lidar with Orthogonal Polarization (CALIOP) product (Winker et al. 2006) based on Cloud-Aerosol Lidar and Infrared Pathfinder Satellite Observation (CALIPSO).

During JMA/MSC's operations with the product based on the time-proven algorithm approach, the organization has also considered the maximum likelihood estimation algorithm developed by the National Oceanic and Atmospheric Administration under the National Environmental Satellite, Data, and Information Service (NOAA/NESDIS) to improve JMA/MSC's cloud top height estimation accuracy. The Algorithm Theoretical Basis Document (ATBD) of NOAA/NESDIS is available online in relation to the ABI Cloud Height Algorithm (ACHA) (Heidinger 2013) designed for the Advanced Baseline Imager (ABI) (Schmit et al. 2005) units on board the Geostationary Operational Environmental Satellite - R series (GOES-R). The specifications of the ABI are almost identical to those of the Advanced Himawari Imager (AHI) on board Himawari-8, for which the ACHA is considered appropriate.

For implementation of the ACHA, JMA/MSC originally developed software based on the NOAA/NESDIS ATBD for appropriate operation with its in-house computer environment rather than using the software package distributed by NOAA/NESDIS. In addition to this proprietary implementation, the cloud

Satellite Application and Analysis Division, Data Processing Department, Meteorological Satellite Center

(Received 6 September 2018, accepted 12 April 2019)

radiative model in the cloud top height estimation algorithm is expanded to a two-layer cloud model rather than straightforward implementation based on the ATBD for the ACHA. This model is expected to produce high estimation accuracy when the AHI observes thin upper-layer cloud and thick lower-layer cloud simultaneously. The mean error was improved to -420 m and the correlation coefficient to 0.82.

ACHA cloud top height estimation runs together with pre-processed cloud type and the cloud phase product based on the GOES-R algorithm. These cloud type and cloud phase products are processed ahead of cloud height estimation. The cloud type and phase algorithm is implemented with no changes to its original form, and is detailed in ABI Cloud Type/Phase Algorithm ATBD (Pavolonis 2010a) (see the next chapter). Chapter 3 focuses on two-layer cloud model expansion, as the cloud top height estimation process (except for two-layer cloud model expansion) is similar to that of the ATBD for the ACHA. Chapter 4 describes cloud top height evaluation using CALIOP cloud top height information.

2. Cloud type/phase product

The ATBD for the ABI Cloud Type/Phase Algorithm (ACTA) used to estimate cloud type and phase for GOES-R ABI (Pavolonis 2010a) is available online. JMA/MSC has incorporated the algorithm into its computer environment and applies its parameters without change. It is appropriate for use because the ABI on GOES-R and the AHI on Himawari-8 essentially have the same specifications other than certain wavelength values. However, the central wavelengths and response functions differ slightly, while the 7.3, 8.6, 11.2 and 12.4 μm bands used in ACTA are almost the same. A brief description of the algorithm is given in Section 2.1. For more information on the algorithm, see the ATBD for the ACTA (Pavolonis 2010a) released by NOAA/NESDIS.

2.1 Cloud Type/Cloud Phase Algorithm

The cloud type/phase algorithm for the ABI is mainly based on cloud emissivity ε and β values, allowing estimation of cloud particle types and phases. For cloud emissivity calculation, cloud radiative transfer is set as per Eq. 1.

$$R_{\mathrm{obs}}(\lambda) = \varepsilon(\lambda)R_{\mathrm{ac}}(\lambda) + \tau_{\mathrm{ac}}(\lambda)\varepsilon(\lambda)B(\lambda,T) + R_{\mathrm{clr}}(\lambda)\big(1-\varepsilon(\lambda)\big) \qquad \text{(Eq. 1)}$$

λ: Observation wavelength
R_{obs}: Observed radiance
R_{ac}: Atmospheric radiance above cloud
R_{clr}: Clear sky radiance
τ_{ac}: Atmospheric transmittance above cloud
ε: Cloud emissivity
B: Planck function
T: Cloud temperature

Eq. 1 can be transformed for cloud emissivity ε as per Eq. 2.

$$\varepsilon(\lambda) = \frac{R_{\mathrm{obs}}(\lambda)-R_{\mathrm{clr}}(\lambda)}{[B(\lambda,T)\tau_{\mathrm{ac}}(\lambda)+R_{\mathrm{ac}}(\lambda)]-R_{\mathrm{clr}}} \qquad \text{(Eq. 2)}$$

Cloud type and phase information cannot be retrieved from single emissivity values of one wavelength. Multiplex wavelengths need to be combined to determine the information. This algorithm utilizes the parameter β (Inoue 1987, Parol et al. 1991, Giraud et al. 1997, Heidinger and Pavolonis 2009), which expresses the information of two wavelengths (λ_1, λ_2).

$$\beta_{\mathrm{obs}} = \frac{\ln[1-\varepsilon(\lambda_1)]}{\ln[1-\varepsilon(\lambda_2)]} = \frac{\tau_{\mathrm{abs}}(\lambda_1)}{\tau_{\mathrm{abs}}(\lambda_2)} \qquad \text{(Eq. 3)}$$

β_{obs}: β value from observation

Eq. 3 is interpreted as the ratio of the effective absorption optical depth τ_{abs} between two wavelengths in the infrared region. Aside from this equation, the ratio of normalized extinction coefficients between two wavelengths was shown to be theoretically determinable from the single scattering albedo ω, the asymmetry parameter g and the extinction cross section σ_{ext} by Parol et al. (1991) as per Eq. 4.

$$\beta_{\mathrm{theo}} = \frac{(1.0-\omega(\lambda_1)g(\lambda_1))\sigma_{\mathrm{ext}}(\lambda_1)}{(1.0-\omega(\lambda_2)g(\lambda_2))\sigma_{\mathrm{ext}}(\lambda_2)} \qquad \text{(Eq. 4)}$$

β_{theo}: β based on theoretical calculation

Parol et al. (1991) and Pavolonis (2010b) demonstrated that β_{obs} is a good approximation for β_{theo} in the infrared region as per Eq. 5.

$$\beta_{\mathrm{obs}} \approx \beta_{\mathrm{theo}} \qquad \text{(Eq. 5)}$$

In this way, β has the advantage of combining observed quantity with theoretical cloud microphysics. For

example, $\beta(8.5, 11)$ for 8.5 and 11 μm has different values for water droplets and ice particles with every effective radius shown in Fig. 1 (a), indicating its information content on cloud particle phase. Meanwhile, $\beta(12, 11)$ for 12 and 11 μm provides information on cloud particle effective radius, although it provides little information about the cloud particle phase shown in Fig. 1 (b). The values in parentheses for β are central wavelengths for each band. ACTA incorporates information on β for different band pairs.

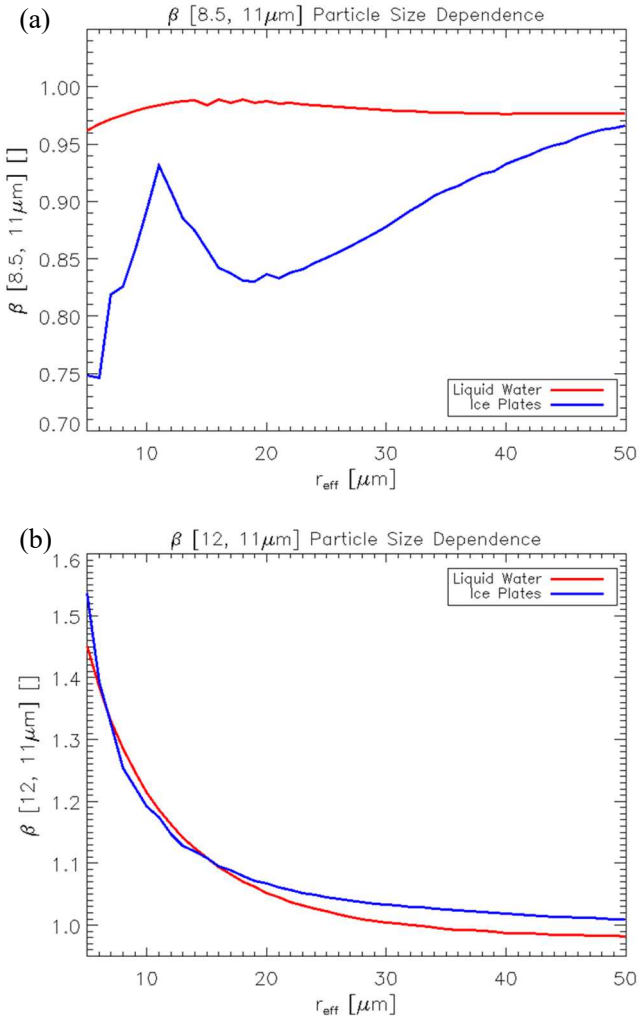

Fig. 1: Difference in β between liquid water and ice plates for effective radius r_{eff}
(a) $\beta(8.5, 11)$ (b) $\beta(12, 11)$
(Quoted from NOAA/NESDIS Cloud Type/Phase ATBD (Pavolonis 2010a) p. 27.)

In actual processing, the band pairs for β calculation are:
i. $\beta(7.3, 11.2)$
ii. $\beta(8.6, 11.2)$
iii. $\beta(12.4, 11.2)$

These β values are calculated with conditions such as cloud location at the tropopause level in the same way as emissivity values, and both are used in overall multilayer cloud testing, overall ice cloud testing, sub-classification ice cloud testing, mixed-phase testing and supercooled liquid-water testing. The related decision tree is shown in Fig. 2. The cloud particle phase is divided into the categories of liquid water, supercooled water, mixed and ice based on cloud types (Pavolonis 2010a).

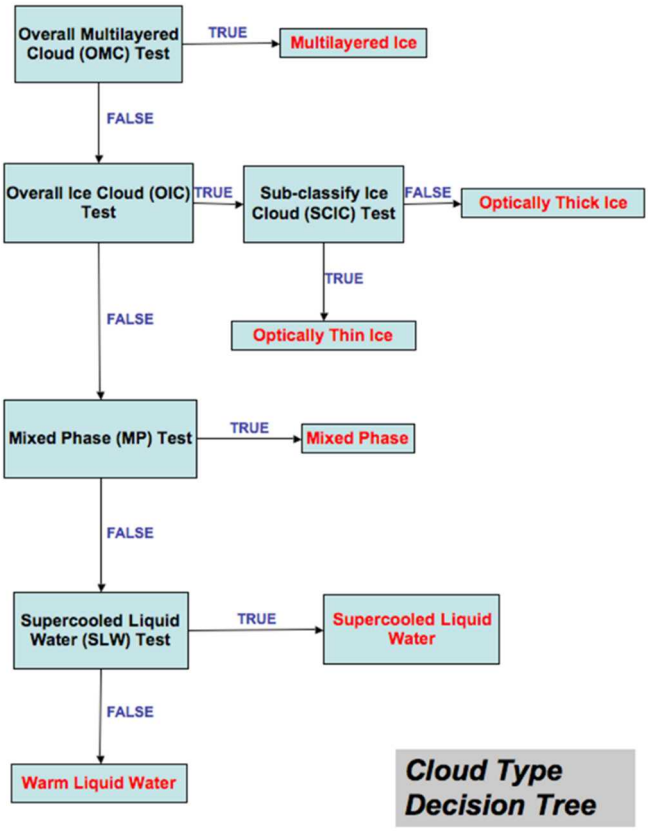

Fig. 2: Cloud type decision tree
(From NOAA/NESDIS Cloud Type/Phase ATBD (Pavolonis 2010a) p. 64)

2.2 Input data for cloud type/phase and examples of related output

The inputs for cloud type/phase processing are:
i. Himawari-8 radiance data (7.3, 8.6, 11.2, 12.4 μm)
ii. Radiative transfer calculated radiance data (7.3, 8.6, 11.2, 12.4 μm)
iii. Surface emissivity data (7.3, 8.6, 11.2, 12.4 μm)
iv. Cloud mask data (Imai et al. 2016)
Radiative transfer calculation involves the use of RTTOV (Hocking et al. 2015), and the input data are from the JMA global forecast model. Surface emissivity data come from

RTTOV ancillary information.

Table 1 shows output data, and an example from 03 UTC on August 1 2017 is shown in Fig. 3.

Table 1: Cloud type/phase output elements

Cloud Type	Cloud Phase
Warm Liquid Water	Liquid Water Phase
Supercooled Liquid Water	Supercooled Water Phase
Mixed Phase	Mixed Phase
Optically Thick Ice	Ice Phase
Optically Thin Ice	
Multilayered Ice	

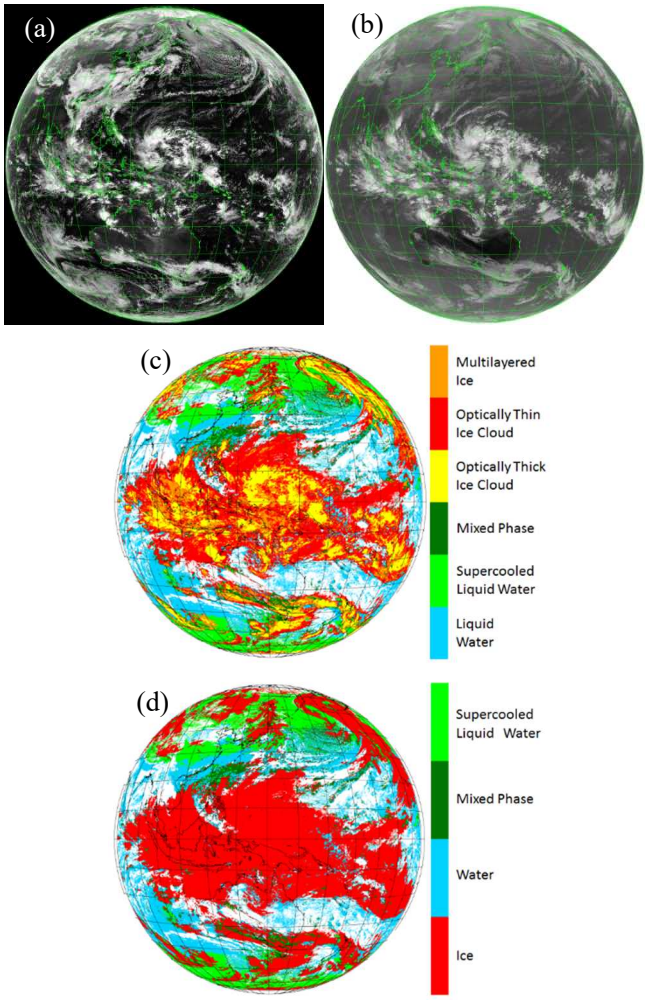

Fig. 3: Cloud type/phase example from 03 UTC on February 1 2017
(a) 0.64 μm image (b) 10.4 μm image
(c) Cloud type (d) Cloud phase

3. Cloud top height product

The cloud top height estimation algorithm developed by JMA/MSC is based on the GOES-R ABI cloud top height estimation algorithm (ACHA) (Heidinger 2013). The ACHA uses a single-layer cloud radiative model, which JMA/MSC expanded to two layers. This chapter describes the optimal estimation method used in the ACHA and the expansion for this two-layer model.

3.1 ACHA optimal estimation

Cloud top height estimation involves the optimal method used in the GOES-R cloud top height estimation algorithm as described by Rodgers (1976). The observed radiance follows Gaussian probability density distribution close to estimated radiance, and estimated values such as brightness temperature also follow such distribution close to the first-guess value. Physical values corresponding to the maxima for the product of these distributions are taken as optimal estimations. Eq. 6 expresses the probability density distribution of an estimated physical value.

$$P_{\mathrm{x}}(x) = \frac{1}{(2\pi)^{\frac{n_{\mathrm{x}}}{2}}|S_{\mathrm{a}}|^{\frac{1}{2}}} \exp\left\{-\frac{1}{2}(x-x_{\mathrm{a}})^{\mathrm{T}} S_{\mathrm{a}}{}^{-1}(x-x_{\mathrm{a}})\right\} \quad \text{(Eq. 6)}$$

P_{x}: Probability density distribution of estimated value
x_{a}: Vector of first-guess value
x: Vector of estimated value
$\mathrm{S_a}$: Variance matrix of error between estimated value and first-guess value
n_{x}: Dimension of x
$|S_{\mathrm{a}}|$: Determinant of $\mathrm{S_a}$

Eq. 7 expresses the probability density distribution of the observed radiance close to the estimated radiance, which comes from the radiative transfer model.

$$P_{\mathrm{y}}(y) = \frac{1}{(2\pi)^{\frac{n_{\mathrm{y}}}{2}}|S_{\mathrm{y}}|^{\frac{1}{2}}} \exp\left\{-\frac{1}{2}(y-f(x))^{\mathrm{T}} S_{\mathrm{y}}{}^{-1}(y-f(x))\right\} \quad \text{(Eq. 7)}$$

P_{y}: Probability density distribution of observed radiance
y: Vector of observed radiance
$f(x)$: Vector of estimated radiance based on the radiative transfer model
$\mathrm{S_y}$: Variance matrix of error between observed and estimated radiances based on the radiative transfer model

n_y: Dimension of y

$|S_y|$: Determinant of S_y

Eq. 8 shows the product of Eq. 6 and Eq. 7.

$$P_x(x)P_y(y) = \frac{1}{(2\pi)^{\frac{n_x+n_y}{2}}|S_a|^{\frac{1}{2}}|S_y|^{\frac{1}{2}}} \exp\left\{-\frac{1}{2}(x-x_a)^T S_a^{-1}(x-x_a) - \frac{1}{2}\left(y-f(x)\right)^T S_y^{-1}\left(y-f(x)\right)\right\} \quad \text{(Eq. 8)}$$

The estimated value gives the maximum for Eq. 8 with optimal estimation as shown in Fig. 4, where the dashed blue line represents the probability density distribution of estimated values close to the first-guess value. The dashed red line represents the probability density function of observed values close to the estimated radiance based on the radiative transfer model. The solid green solid line represents the product of both distributions. The estimation value is the x figure representing maximum probability density.

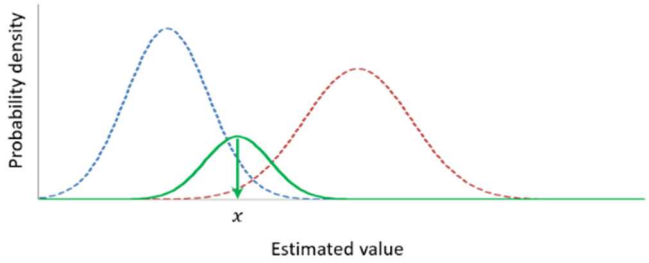

Fig. 4: Conceptual diagram of optimal estimation
The dashed blue line represents the probability density distribution of estimated values close to the first-guess value. The dashed red line represents the probability density function of observed values close to the estimated radiance based on the radiative transfer model. The solid green line represents the product of both distributions. The estimation value is the x figure representing maximum probability density.

Determination of the maximum value for Eq. 8 allows minimization of the value φ in Eq. 9, which is an exponent part of Eq. 8.

$$\varphi = (x-x_a)^T S_a^{-1}(x-x_a) + \left(y-f(x)\right)^T S_y^{-1}\left(y-f(x)\right) \quad \text{(Eq. 9)}$$

Eq. 9 is often referred to as the cost function, and corresponds to Eq. 6 in the ATBD for the ACHA (Heidinger 2013). The Newtonian method is utilized to determine the local minimal value of Eq. 9. The displacement of x is calculated using Eq. 10 in the Newtonian method.

$$\delta x = -\left(\frac{\partial^2}{\partial x^2}\varphi\right)^{-1}\frac{\partial}{\partial x}\varphi \quad \text{(Eq. 10)}$$

The first-order derivative term of Eq. 10 is transformed to Eq. 11 using Eq. 9. The second-order derivative term is incorporated to form Eq. 13, and corresponds to a Hessian matrix. It is also equivalent to the S_x value of Eq. 8 in the ATBD for the ACHA (Heidinger 2013), and expresses the variance matrix of the estimation vector x.

$$\frac{\partial}{\partial x}\varphi = S_a^{-1}(x-x_a) - K^T S_y^{-1}\left(y-f(x)\right) \quad \text{(Eq. 11)}$$

$$K = \frac{\partial}{\partial x}f(x) \quad \text{(Eq. 12)}$$

$$\frac{\partial^2}{\partial x^2}\varphi \cong S_a^{-1} + K^T S_y^{-1} K \quad \text{(Eq. 13)}$$

Eq. 10 is transformed to Eq. 14 using Eq. 11 and Eq. 13. Eq. 14 corresponds to Eq. 7 in the ATBD for the ACHA (Heidinger 2013).

$$\delta x = \left(S_a^{-1} + K^T S_y^{-1} K\right)^{-1}\left(S_a^{-1}(x_a - x) + K^T S_y^{-1}\left(y-f(x)\right)\right) \quad \text{(Eq. 14)}$$

Marks and Rodgers (1993) discussed whether optimal estimation converges using Eq. 15, as observed in the ACHA approach. n_x represents the dimension of x.

$$\delta x S_x^{-1}\delta x \ll n_x \quad \text{(Eq. 15)}$$

These are the optimal estimations used in the ACHA, and the JMA/MSC cloud top height estimation product also involves this technique.

3.2 Expansion from a single-layer cloud model to a two-layer cloud model

A single-layer cloud model is adopted in the ATBD for the ACHA (Heidinger 2013). JMA/MSC expanded the single-layer cloud model to a two-layer version based on the ACHA as per Eq. 16, with the related concept illustrated

in Fig. 5. This simple modeling considers only upward radiation in the interests of reducing calculation cost.

$$f = R_{ac} + \tau_{ac}\varepsilon_{c1}B(T_{c1}) + \tau_{ac}(1-\varepsilon_{c1})R_m + \tau_{ac}(1-\varepsilon_{c1})\tau_m\varepsilon_{c2}B(T_{c2}) + \tau_{ac}(1-\varepsilon_{c1})\tau_m(1-\varepsilon_{c2})R_b + \tau_{ac}(1-\varepsilon_{c1})\tau_m(1-\varepsilon_{c2})\tau_b\varepsilon_{srf}B(T_{srf}) \quad \text{(Eq. 16)}$$

ε_{c1}: Emissivity from the first cloud layer
ε_{c2}: Emissivity from the second cloud layer
ε_{sfc}: Surface emissivity
R_{ac}: Radiation from air above the first cloud layer
R_m: Radiation from air between the first and second cloud layers
R_b: Radiation from air under the second cloud layer
τ_{ac}: Atmospheric transmittance above the first cloud layer
τ_m : Atmospheric transmittance between the first and second cloud layers
τ_b : Atmospheric transmittance under the second cloud layer
$B(T)$: Planck function at temperature T
T_{c1}: Cloud temperature at the first layer
T_{c2}: Cloud temperature at the second layer
T_{srf}: Ground surface or sea surface temperature

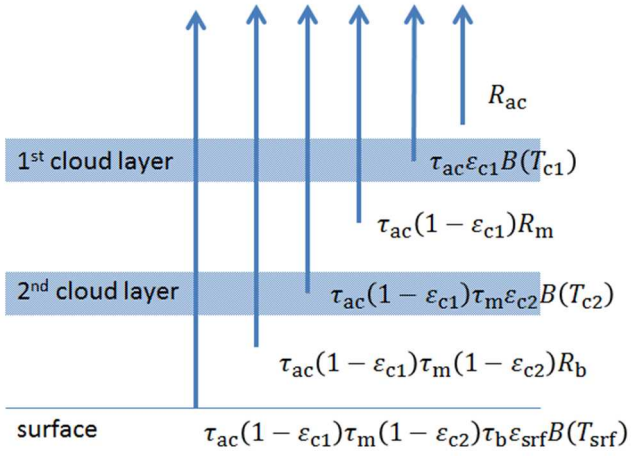

Fig. 5: The expanded JMA/MSC two-layer cloud model

The vector of observed radiance is expressed by Eq. 17, the vector of estimation is expressed by Eq. 18, the vector of the first-guess value is expressed by Eq. 19, and the variance matrix for the first-guess error is expressed by Eq. 20. Values in parentheses represent central wavelengths for each band. These vectors and matrix values are expanded for two-layer cloud modeling. For example, the components of BTD $(11.2-8.6)$, BT (6.2) and BT (7.3) in Eq. 17 are the expanded parts in the observed radiance vectors. The BTD $(11.2-8.6)$ component with a brightness temperature difference of $11.2-8.6$ μm is expected to support effective cirrus cloud detection and the provision of information on cloud microphysics. The 6.2 and 7.3 μm bands are focused on water vapor absorption, and are expected to support effective cirrus cloud detection. In Eq. 17, BT represents brightness temperature and BTD represents brightness temperature difference. The first-guess values and related standard deviations are shown in Tables 2 and 3. In Table 3 of the ATBD for the ACHA based on Heidinger and Pavolonis (2009), the first-guess and standard deviation values for the expanded two-layer cloud model of JMA/MSC are determined by comparing Himawari-8 and CALIPSO cloud top heights. The first cloud layer is used as the cloud top when retrieved emissivity $\varepsilon_{c1}(11.2)$ is greater than 0.005. For values equal to or lower than this, the second cloud layer is used.

$$y = \begin{pmatrix} \mathrm{BT}(11.2) \\ \mathrm{BTD}(11.2-12.4) \\ \mathrm{BTD}(11.2-13.3) \\ \mathrm{BTD}(11.2-8.6) \\ \mathrm{BT}(6.2) \\ \mathrm{BT}(7.3) \end{pmatrix} \quad \text{(Eq. 17)}$$

$$x = \begin{pmatrix} T_{c1} \\ \varepsilon_{c1}(11.2) \\ \beta_{c1}(12.4,11.2) \\ T_{c2} \\ \varepsilon_{c2}(11.2) \\ \beta_{c2}(12.4,11.2) \end{pmatrix} \quad \text{(Eq. 18)}$$

$$x_a = \begin{pmatrix} T_{c1\_ap} \\ \varepsilon_{c1\_ap}(11.2) \\ \beta_{c1\_ap}(12.4,11.2) \\ T_{c2\_ap} \\ \varepsilon_{c2\_ap}(11.2) \\ \beta_{c2\_ap}(12.4,11.2) \end{pmatrix} \quad \text{(Eq. 19)}$$

$$S_a = \begin{pmatrix} \sigma^2_{T_{c1\_ap}} & 0.0 & 0.0 & 0.0 & 0.0 & 0.0 \\ 0.0 & \sigma^2_{\varepsilon_{c1\_ap}(11.2)} & 0.0 & 0.0 & 0.0 & 0.0 \\ 0.0 & 0.0 & \sigma^2_{\beta_{c1\_ap}(12.4,11.2)} & 0.0 & 0.0 & 0.0 \\ 0.0 & 0.0 & 0.0 & \sigma^2_{T_{c2\_ap}} & 0.0 & 0.0 \\ 0.0 & 0.0 & 0.0 & 0.0 & \sigma^2_{\varepsilon_{c2\_ap}(11.2)} & 0.0 \\ 0.0 & 0.0 & 0.0 & 0.0 & 0.0 & \sigma^2_{\beta_{c2\_ap}(12.4,11.2)} \end{pmatrix} \quad \text{(Eq. 20)}$$

Table 2: First-guess values for the first layer on the upper side of the cloud layer

T_{trp} is the tropopause layer temperature from JMA's global forecast model, and $BT(11.2)$ is the brightness temperature observed at the 11.2 μm band.

	T_{c1_ap}	σ_{Tc1_ap}	τ_{14_c1}	$\sigma_{\varepsilon c1\_ap(11.2)}$	$\beta_{c1\_ap}(12.4,11.2)$	$\sigma_{\beta c1\_ap(12.4,11.2)}$
Liquid Water	BT(11.2)	10 K	2.3	0.4	1.3	0.2
Supercooled Liquid Water	BT(11.2)	10 K	2.3	0.1	1.3	0.2
Mixed Phase	BT(11.2)	10 K	2.3	0.1	1.3	0.2
Optically Thick Ice	T_{trp}	10 K	2.3	0.1	1.1	0.2
Optically Thin Ice	T_{trp}	19 K	0.9	0.4	1.1	0.2
Multi-layer Ice	T_{trp}	7 K	1.5	0.4	1.1	0.2

Table 3: First-guess values for the second layer on the lower side of the cloud layer

T_{trp} is the tropopause layer temperature, T_{srf} is the surface temperature from JMA's global forecast model, and $BT(11.2)$ is the brightness temperature observed at the 11.2 μm band.

	T_{c2_ap}	σ_{Tc2_ap}	τ_{14_c2}	$\sigma_{\varepsilon c2\_ap(11.2)}$	$\beta_{c2\_ap}(12.4,11.2)$	$\sigma_{\beta c2\_ap(12.4,11.2)}$
Liquid Water	T_{srf}	10 K	2.3	0.4	1.3	0.2
Supercooled Liquid Water	$0.8T_{srf} + 0.2BT(11.2)$	10 K	2.3	0.1	1.3	0.2
Mixed Phase	$0.8T_{srf} + 0.2T_{trp}$	10 K	2.3	0.1	1.3	0.2
Optically Thick Ice	$0.7T_{srf} + 0.3T_{trp}$	10 K	2.3	0.1	1.1	0.2
Optically Thin Ice	$0.8T_{srf} + 0.2T_{trp}$	19 K	0.9	0.4	1.1	0.2
Multi-layer Ice	$0.8T_{srf} + 0.2T_{trp}$	7 K	1.5	0.4	1.1	0.2

First-guess values of cloud emissivity were calculated using Eq. 21 with τ_{14_c1} (Table 2) and τ_{14_c2} (Table 3). Sat_zen is the satellite zenith angle.

$$\varepsilon_{c\_ap}(11.2) = 1 - \exp\left(-\tau_{14\_c}/\cos(sat\_zen)\right) \quad \text{(Eq. 21)}$$

The parameter τ_{14_c} is the absorption optical depth at the 11.2 μm band. The number 14 represents band 14 (11.2 μm) of the Advanced Himawari Imager. A priori emissivity is calculated from the parameter τ_{14_c} and the satellite zenith angle.

The kernel matrix (k-matrix) of the two-layer cloud model is expressed by Eq. 22.

The expressions of each element in Eq. 22 can be derived in the same way as described for Eq. 14 to Eq. 22 in the ATBD for the ACHA (Heidinger 2013). Part of the element related to β needs to be expressed with a linear regression equation using $\beta(12.4, 11.2)$. For example, calculation of $\beta(13.3, 11.2)$ requires operation with $\beta(12.4, 11.2)$ as per Eq. 23.

$$\beta(13.3, 11.2) = a + b \times \beta(12.4, 11.2) \quad \text{(Eq. 23)}$$

$\beta(6.2, 11.2)$, $\beta(7.3, 11.2)$ and $\beta(8.6, 11.2)$ are expressed in the same way using $\beta(12.4, 11.2)$. Table 4 shows the coefficients a and b for water droplets and ice particles based on the Community Satellite Processing Package (CSPP), which includes the ACHA. The coefficients for water droplets appear to be based on Mie scattering calculation results for a spherical shape, and those for ice particles appear to be based on scattering calculation results for aggregate ice particles. The expanded two-layer cloud model uses water droplet coefficients in consideration of supercooling when the value is ≥ –10°C. For values lower than this, ice particle coefficients are used. The CSPP is a comprehensive satellite data processing package developed by SSEC/CIMSS in the USA, and is available online (http://cimss.ssec.wisc.edu/cspp). As of March 2019, no constants corresponded to the 6.2 and 7.3 μm bands for the ABI/AHI; the expanded two-layer cloud model uses 6.7 μm as a substitute. These constants are expected to be added to the package in the future, and will replace those corresponding to 6.7 μm in the expanded two-layer cloud model.

$$K = \begin{pmatrix} \frac{\partial BT(11.2)}{\partial T_{c1}} & \frac{\partial BT(11.2)}{\partial \varepsilon_{c1}(11.2)} & \frac{\partial BT(11.2)}{\partial \beta_{c1}(12.4,11.2)} & \frac{\partial BT(11.2)}{\partial T_{c2}} & \frac{\partial BT(11.2)}{\partial \varepsilon_{c2}(11.2)} & \frac{\partial BT(11.2)}{\partial \beta_{c2}(12.4,11.2)} \\ \frac{\partial BTD(11.2-12.4)}{\partial T_{c1}} & \frac{\partial BTD(11.2-12.4)}{\partial \varepsilon_{c1}(11.2)} & \frac{\partial BTD(11.2-12.4)}{\partial \beta_{c1}(12.4,11.2)} & \frac{\partial BTD(11.2-12.4)}{\partial T_{c2}} & \frac{\partial BTD(11.2-12.4)}{\partial \varepsilon_{c2}(11.2)} & \frac{\partial BTD(11.2-12.4)}{\partial \beta_{c2}(12.4,11.2)} \\ \frac{\partial BTD(11.2-13.3)}{\partial T_{c1}} & \frac{\partial BTD(11.2-13.3)}{\partial \varepsilon_{c1}(11.2)} & \frac{\partial BTD(11.2-13.3)}{\partial \beta_{c1}(12.4,11.2)} & \frac{\partial BTD(11.2-13.3)}{\partial T_{c2}} & \frac{\partial BTD(11.2-13.3)}{\partial \varepsilon_{c2}(11.2)} & \frac{\partial BTD(11.2-13.3)}{\partial \beta_{c2}(12.4,11.2)} \\ \frac{\partial BTD(11.2-8.6)}{\partial T_{c1}} & \frac{\partial BTD(11.2-8.6)}{\partial \varepsilon_{c1}(11.2)} & \frac{\partial BTD(11.2-8.6)}{\partial \beta_{c1}(12.4,11.2)} & \frac{\partial BTD(11.2-8.6)}{\partial T_{c2}} & \frac{\partial BTD(11.2-8.6)}{\partial \varepsilon_{c2}(11.2)} & \frac{\partial BTD(11.2-8.6)}{\partial \beta_{c2}(12.4,11.2)} \\ \frac{\partial BT(6.2)}{\partial T_{c1}} & \frac{\partial BT(6.2)}{\partial \varepsilon_{c1}(11.2)} & \frac{\partial BT(6.2)}{\partial \beta_{c1}(12.4,11.2)} & \frac{\partial BT(6.2)}{\partial T_{c2}} & \frac{\partial BT(6.2)}{\partial \varepsilon_{c2}(11.2)} & \frac{\partial BT(6.2)}{\partial \beta_{c2}(12.4,11.2)} \\ \frac{\partial BT(7.3)}{\partial T_{c1}} & \frac{\partial BT(7.3)}{\partial \varepsilon_{c1}(11.2)} & \frac{\partial BT(7.3)}{\partial \beta_{c1}(12.4,11.2)} & \frac{\partial BT(7.3)}{\partial T_{c2}} & \frac{\partial BT(7.3)}{\partial \varepsilon_{c2}(11.2)} & \frac{\partial BT(7.3)}{\partial \beta_{c2}(12.4,11.2)} \end{pmatrix}$$

(Eq. 22)

Table 4: Coefficients of a and b for β regression equations $\beta(\lambda_1, \lambda_2)$ is expressed by the regression equation below.
$\beta(\lambda_1, \lambda_2) = \mathrm{a} + \mathrm{b} \times \beta(12.4, 11.2)$

	a (ice phase)	b (ice phase)	a (water phase)	b (water phase)
$\beta(6.2, 11.2)$	0.95539	0.07902	0.268115	0.702683
$\beta(7.3, 11.2)$	0.95539	0.07902	0.268115	0.702683
$\beta(8.6, 11.2)$	1.40457	-0.39163	0.930569	0.048857
$\beta(13.3, 11.2)$	-0.02641	1.08386	-0.728113	1.743389

The variance matrix of errors for the two-layer cloud model is expressed by Eq. 24, and Eq. 25 is the expression for each element. The values for σ_{instr} and σ_{clr} are shown in Table 5. σ_{hetero} in Eq. 25 is the standard deviation of brightness temperature for the 3 x 3 pixels around the target pixel. Table 5 shows the variance for clear sky radiance and related values based on Himawari-8 data and radiative transfer calculation using RTTOV.

$$S_{\mathrm{y}} = \begin{pmatrix} \sigma^2_{\mathrm{BT}(11.2)} & 0.0 & 0.0 & 0.0 & 0.0 & 0.0 \\ 0.0 & \sigma^2_{\mathrm{BTD}(11.2-12.4)} & 0.0 & 0.0 & 0.0 & 0.0 \\ 0.0 & 0.0 & \sigma^2_{\mathrm{BTD}(11.2-13.3)} & 0.0 & 0.0 & 0.0 \\ 0.0 & 0.0 & 0.0 & \sigma^2_{\mathrm{BTD}(11.2-8.6)} & 0.0 & 0.0 \\ 0.0 & 0.0 & 0.0 & 0.0 & \sigma^2_{\mathrm{BT}(6.2)} & 0.0 \\ 0.0 & 0.0 & 0.0 & 0.0 & 0.0 & \sigma^2_{\mathrm{BT}(7.3)} \end{pmatrix} \quad \text{(Eq. 24)}$$

$$\sigma^2 = \sigma^2_{\mathrm{instr}} + \big(1 - \varepsilon_{\mathrm{c}}(11.2)\big)\sigma^2_{\mathrm{clr}} + \sigma^2_{\mathrm{hetero}} \quad \text{(Eq. 25)}$$

Table 5: Standard deviation for S_y
$\mathrm{BT}(11.2)$ is brightness temperature at 11.2 μm, and $\mathrm{BTD}(11.2 - 12.4)$ is the brightness temperature difference between 11.2 and 12.4 μm as per other wavelengths.

	σ_{instr}	σ_{clr}(Ocean)	σ_{clr}(Land)
$\mathrm{BT}(11.2)$	1.0	6.603	4.016
$\mathrm{BTD}(11.2 - 12.4)$	0.5	0.75	0.427
$\mathrm{BTD}(11.2 - 13.3)$	1.0	0.796	0.83
$\mathrm{BTD}(11.2 - 8.6)$	0.5	1.36	0.78
$\mathrm{BT}(6.2)$	1.0	8.865	6.979
$\mathrm{BT}(7.3)$	1.0	7.656	5.028

3.3 Cloud top height product input and output data

Input data:
i. Himawari-8 observation data (6.2, 7.3, 8.6, 11.2, 12.4, 13.3 μm)
ii. Radiative transfer calculation data (6.2, 7.3, 8.6, 11.2, 12.4, 13.3 μm and surface emissivity)
iii. Sea surface temperature
iv. Cloud mask data
v. Cloud type data

RTTOV 11 (Hocking et al. 2015) is utilized for radiative transfer calculation. The inputs for RTTOV 11 come from JMA global forecast model data.

Output data:
i. Cloud top temperature (K), cloud top height (m), cloud top pressure (hPa)
ii. Cloud top emissivity (11.2 μm)
iii. Cloud top $\beta(12.4, 11.2)$

Examples of output data are shown in Fig. 6.

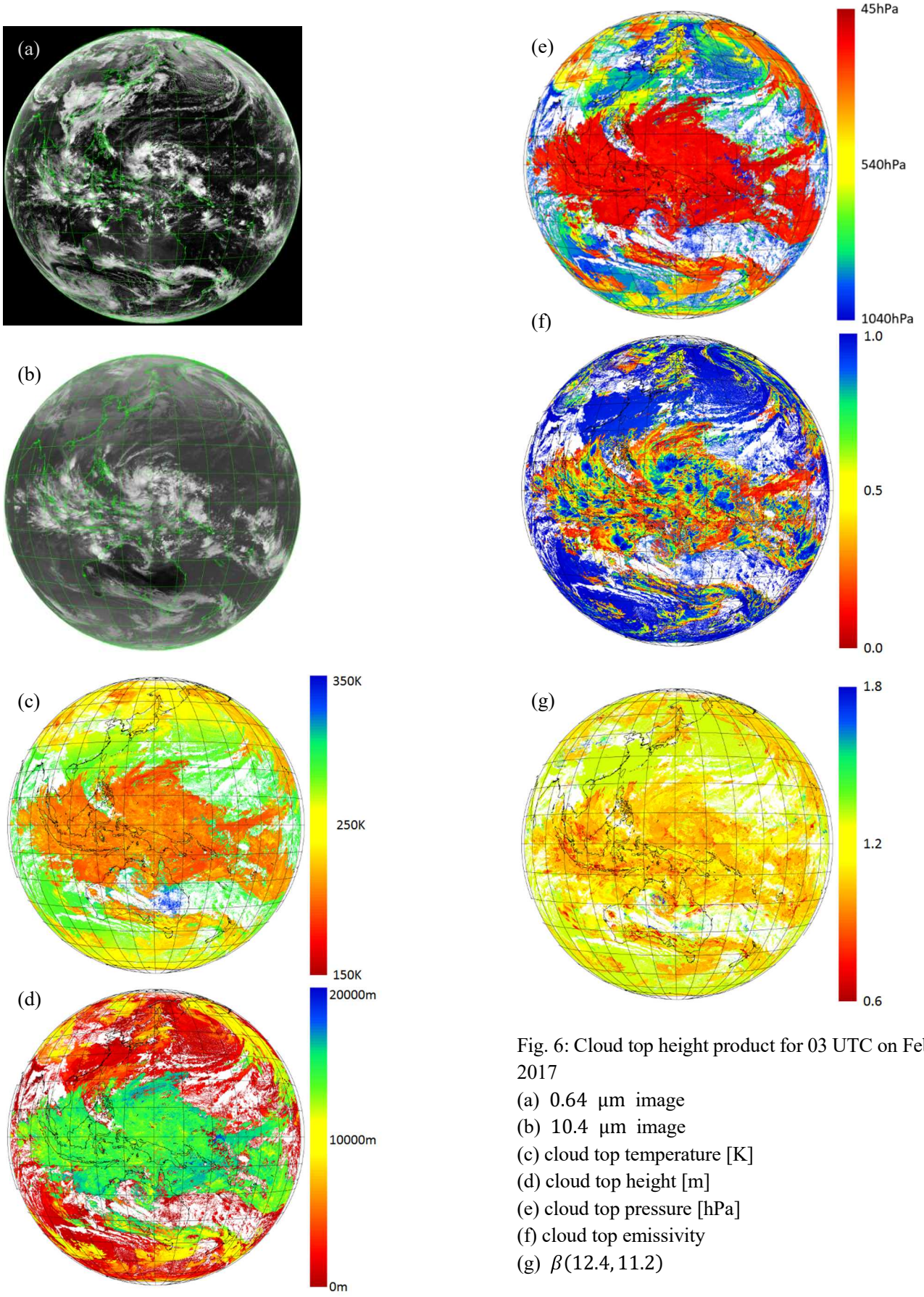

Fig. 6: Cloud top height product for 03 UTC on February 1 2017
(a) 0.64 μm image
(b) 10.4 μm image
(c) cloud top temperature [K]
(d) cloud top height [m]
(e) cloud top pressure [hPa]
(f) cloud top emissivity
(g) $\beta(12.4, 11.2)$

4. Cloud top height evaluation using CALIOP

The CALIOP Level 2 product (Winker et al. 2006) is utilized to evaluate the JMA/MSC cloud top height product. As CALIOP observes both cloud and aerosols, the data used for evaluation are high in quality and cloud-flagged. In the collocation process, the nearest data within five minutes are matched.

The first layer of the layer top altitude in CALIOP L2 data is utilized for evaluation. The results of comparison carried out for February 2017 are shown in Fig. 7 and 8. The correlation coefficient of 0.82 for the test product is better than the 0.75 value for the operational product, and its mean error is also better at –420 m. vs –903 m. However, the test product results include overestimation for upper-layer cloud height. Figure 8 shows histograms of cloud top height; while operational estimation shows high frequencies around 5 and 10 km, test height estimation exhibits no such anomalies and has a distribution pattern rather similar to that of CALIOP.

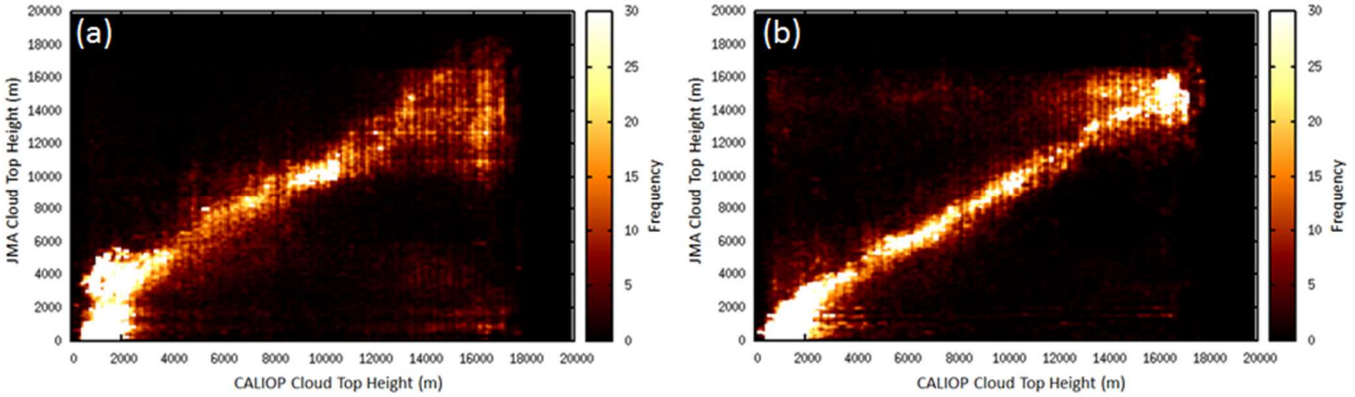

Fig. 7: Scatter plots of histograms for February 2017
CALIOP cloud top height is from the first layer of layer top altitude in the CALIOP data file.
(a) Scatter plots for the operational CALIOP layer top altitude product. The correlation coefficient is 0.75.
(b) Scatter plots for the test product based on the GOES-R algorithm to the CALIOP layer top altitude. The correlation coefficient is 0.82.

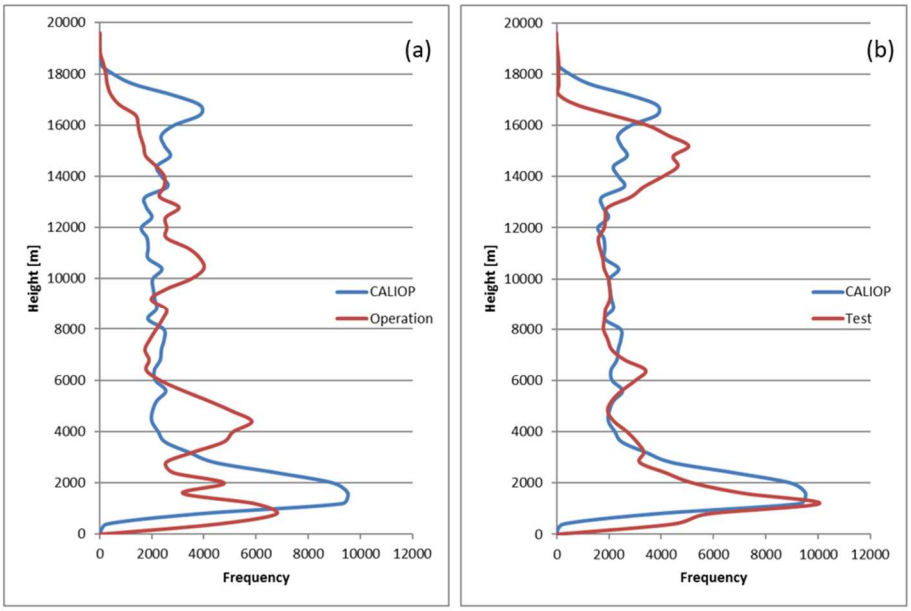

Fig. 8: Histograms of cloud top height for the operational and test products based on the GOES-R algorithm for the CALIOP layer top altitude for February 2017
(a) Operational product: red line; CALIOP layer top altitude: blue line
(b) Test product: red line; CALIOP layer top altitude: blue line

For the two-layer cloud situation, cloud top height estimation based on the GOES-R algorithm is superior to operational estimation. An example from 15 UTC on February 13 2017 is shown below. Figures 9 (a), (b) and (c) show a 10.4 μm image, operational cloud top height and test cloud top height, respectively. The arrows show the CALIPSO path from A to B. Mid-level cloud types such as altocumulus and altostratus are seen in Fig. 9 (a), but cirrus cloud is unclear. The operational product in Fig. 9 (b) shows lower cloud top height than the test product based on the GOES-R algorithm in Fig. 9 (c) along A – B. Figure 9 (d) shows a cross section of CALIOP backscatter intensity at 532 nm along A – B. Thin cirrus clouds are present around 16 km with weak intensity, and mid-level clouds are present around 6 km with strong intensity. Figure 9 (d) also shows CALIOP cloud top height (cyan dots), estimated cloud top height from the test product based on the GOES-R algorithm (red dots) and the same from the operational product (yellow dots).The red dots representing the test product are closer to CALIOP cloud top height than the yellow dots of the operational product. Cloud top height estimation with the test product is better in the two-layer cloud situation than with the operational product.

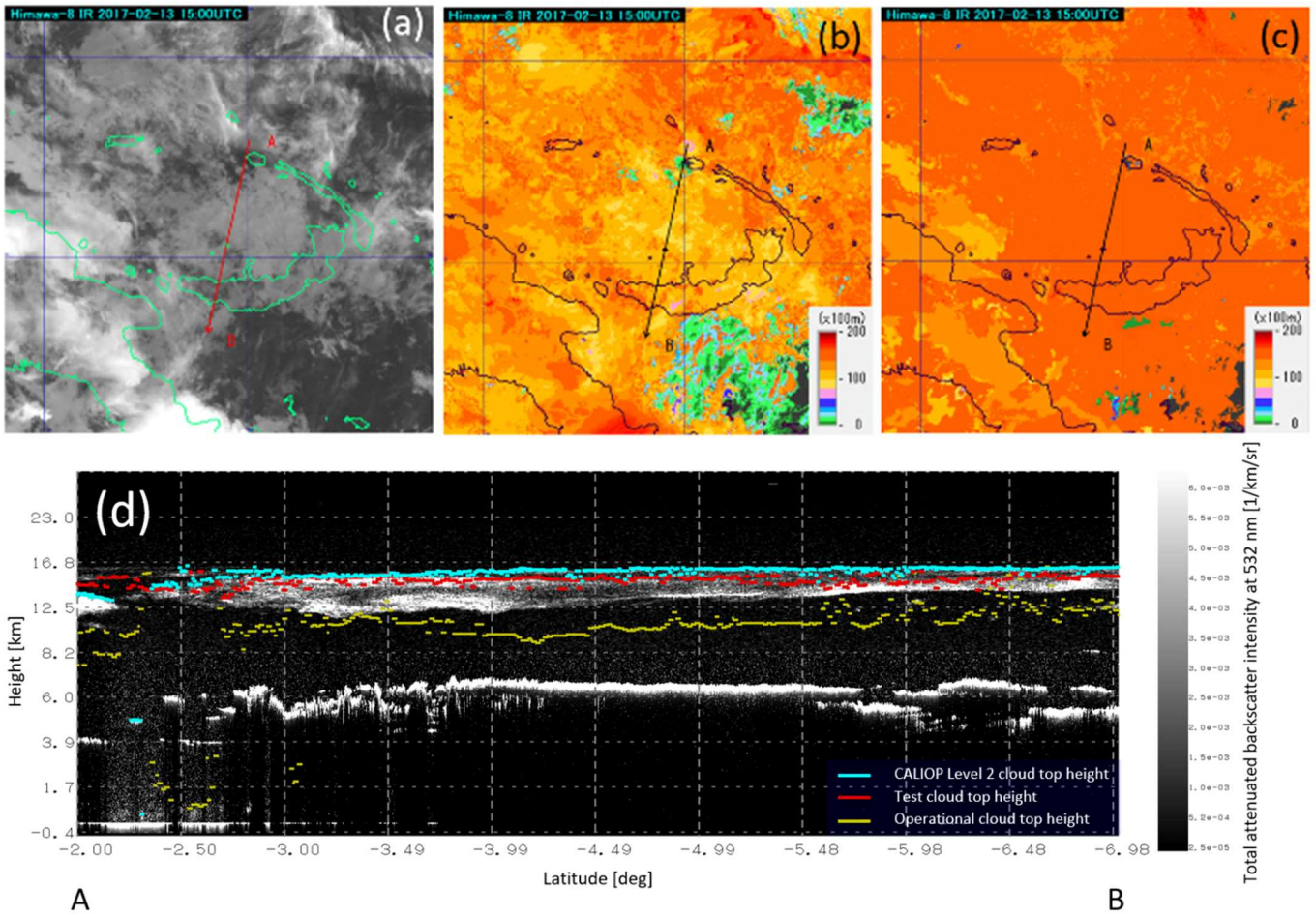

Fig. 9: Operational and test cloud top height results for 15 UTC on February 13 2017
The path of CALIPSO's movement from A to B in these images is shown by red or black arrows.
(a) 10.4 μm image of an area near Papua New Guinea
(b) Operational cloud top height
(c) Test cloud top height
(d) Cross section of CALIOP backscattering intensity at 532 nm with cloud top height estimation results. Cyan dots show cloud top height from the CALIOP Level 2 product. Red and yellow dots show cloud top height estimation results from the test and operational products, respectively. On the horizontal axis, -2.0 degrees represents a southern latitude of 2.0 degrees and corresponds to A in Fig. 9 (a), (b) and (c). In the same way, -5.0 degrees represents a southern latitude of 5.0 degrees and corresponds to B in Fig. 9 (a), (b) and (c).

5. Summary

JMA/MSC tested the cloud top height algorithm based on the GOES-R algorithm to support improved accuracy in cloud top height estimation. The cloud type/phase algorithm is implemented as per the ATBD, but JMA/MSC expanded the cloud top height algorithm of GOES-R from a single-layer model to two layers for improved estimation accuracy. As a result, the cloud top height correlation coefficient between the JMA/MSC test product and the CALIOP Level 2 cloud product improved to 0.82, and the mean error of cloud top height also improved to -420 m. Histogram representation of cloud top height for February 2017 showed that the distribution pattern of the JMA/MSC test product was similar to that of CALIOP, although unnaturally high frequencies were observed around 5 and 10 km in the operational product. Nevertheless, the histogram distribution pattern of the JMA/MSC test product was superior to that of the operational product, albeit with some overestimation of cloud top height in the upper layer (an issue currently under investigation). For two-layer situations, such as those in which cirrus and mid- or low-level cloud are present simultaneously, cloud top height estimation accuracy was superior to that of the operational cloud top height product.

The overestimation observed needs to be addressed in future work. Clear sky co-variance errors related to errors in estimation for clear sky radiance also need to be considered, as current consideration is limited exclusively to variance errors. Certain parameters for the ABI also need to be modified to fit the AHI.

Acknowledgements

The author gratefully acknowledges the two anonymous reviewers who provided helpful comments on this manuscript, and also thanks the NASA Langley Research Center Atmospheric Science Data Center for providing the CALIOP data used in the study.

References

Bessho, K., K. Date, M. Hayashi, A. Ikeda, T. Imai, H. Inoue, Y. Kumagai, T. Miyakawa, H. Murata, T. Ohno, A. Okuyama, R. Oyama, Y. Sasaki, Y. Shimazu, K. Shimoji, Y. Sumida, M. Suzuki, H. Taniguchi, H. Tsuchiyama, D. Uesawa, H. Yokota, and R. Yoshida, 2016: An introduction to Himawari-8/9 -- Japan's new-generation geostationary meteorological satellites. J. Meteorol. Soc. Japan, 94, 151-183.

Giraud, V., J. C. Buriez, Y. Fouquart, F. Parol, and G. Seze, 1997: Large-scale analysis of cirrus clouds from AVHRR data: Assessment of both a microphysical index and the cloud-top temperature. J.Appl.Meteorol., 36, 664-675.

Heidinger A. K.,2013: Algorithm Theoretical Basis Document ABI Cloud Height. URL : https://www.star.nesdis.noaa.gov/goesr/docs/ATBD/Cloud_Height.pdf (accessed 2019-03-25).

Heidinger, A. K. and M. J. Pavolonis, 2009: Nearly 30 years of gazing at cirrus clouds through a split-window. Part I: Methodology. J. Appl. Meteorol. and Climatology, 48(6), 110-1116.

Hocking, J., P. J. Rayer, D. Rundle, R. W. Saunders, M. Matricardi, A. Geer, P. Brunel and J. Vidot, 2015: RTTOV v11 Users Guide, NWP-SAF report, Met.Office, UK.

Imai,T., R. Yoshida, 2016: Algorithm theoretical basis for Himawari-8 Cloud Mask Product. Meteorological Satellite Center Technical Note, 61, 1-17

Inoue, T., 1987: A Cloud Type Classification with NOAA 7 Split-Window Measurements. J. Geophys. Res.-Atmos., 92, 3991-4000.

Marks, C. J., and C. D. Rodgers, 1993: A retrieval method for atmospheric composition from limb emission measurements. J. Geophys. Res. , 98, 14939-14953.

Menzel W. P., W. L. Smith, and T. R. Stewart, 1983: Improved Cloud Motion Wind Vector and Altitude Assignment using VAS. J. Appl. Meteorol. , 22, 377-384.

Mouri, K., H. Suzue, R. Yoshida, and T. Izumi, 2016: Algorithm Theoretical Basis Document of Cloud top height product. Meteorological Satellite Center Technical Note, 61, 33-42.

Nieman, S. J., J. Schmetz, W. P. Menzel, 1993: A Comparison of Several Techniques to Assign Heights to Cloud Tracers. J. Appl. Meteorol., 32, 1559-1568.

Parol, F., J. C. Buriez, G. Brogniez, and Y. Fouquart, 1991: Information-Content of Avhrr Channels 4 and

5 with Respect to the Effective Radius of Cirrus Cloud Particles. J.Appl.Meteorol. , 30, 973-984.

Pavolonis, M. J., 2010a: GOES-R Advanced Baseli ne Imager (ABI) Algorithm Theoretical Basis Document For Cloud Type and Cloud Phase. URL : https://www.star.nesdis.noaa.gov/goesr/doc uments/ATBDs/Baseline/ATBD_GOES-R_Cloud_ Phase_Type_v2.0_Sep2010.pdf (accessed : 2019-03-25).

Pavolonis, M. J., 2010b: Advances in extracting cloud composition information from spaceborne infrared radiances: A robust alternative to brightness temperatures. Part I: Theory. J. Appl. Meteorol. Climatol., 49, 1992-2012.

Rodgers, C. D., 1976: Retrieval of atmospheric temperature and composition from remote measurements of thermal radiation. Rev. Geophys. , 14, 609-624.

Schmetz, J., P. Pili, S. Tjemkes, D. Just, J. Kerkmann, S. Rota, and A. Ratier, 2002: An introduction to meteosat second generation (MSG). Bull. Amer. Meteor. Soc., 83, 977-992.

Schmetz, J., K. Holmlund, J. Hoffman, and B. Strauss, 1993: Operational cloud motion winds from Meteosat infrared images. Journal of Applied Meteorology, 32, 1207-1225.

Schmit, T., M. M. Gunshor, W. P. Menzel, J. J. Gurka, J. Li, and A. S. Bachmeier, 2005: Introducing the next-generation Advanced Baseline Imager on GOES-R. Bull. Amer. Meteor. Soc., 86, 1079-1096.

Winker, D. M., C. A. Hostetler, M. A. Vaughan, and A. H. Omar, 2006: Caliop Algorithm Theoretical Basis Document Part 1: CALIOP Instrument, and Algorithms Overview. 20-23.

基本雲プロダクト雲頂高度アルゴリズムの改良とその評価

毛利　浩樹*

要旨

2015 年 7 月に正式に運用を開始したひまわり 8 号/AHI では、雲頂高度推定アルゴリズムに単純内挿法、IR-WV インターセプト法や CO_2 スライシングといった古くから用いられている手法を採用した。この雲頂高度を CALIOP の雲頂高度と比較すると相関係数にして 0.75 程度であった。CALIOP は米国 NASA とフランス CNES によって運用されている CALIPSO という衛星に搭載され、ライダーを用いて雲やエーロゾルを観測している。一方、NOAA は GOES-R/ABI 用に新しい雲頂高度推定手法を準備していた。ひまわり 8 号/AHI と GOES-R/ABI は 0.51 μm と 1.3 μm 帯を除いて非常によく似たイメージャーである。特に赤外バンドはほぼ同等であり、ひまわり 8 号/AHI に GOES-R/ABI 用の雲頂高度推定アルゴリズムを適用するのは容易であろうと考えられた。JMA/MSC はこの新しい概念で作成された GOES-R 雲頂高度推定アルゴリズムを調査し、上層雲と中下層雲が同時に存在するような 2 層構造をとる雲を効果的に取り扱うための拡張も施したアルゴリズムを開発した。その結果、系統的な誤差を示す平均誤差と相関係数が改善した。本報告では、2 層雲モデルへ拡張した雲頂高度推定アルゴリズムについて主に述べるが、雲頂高度推定に必須となる雲タイプと雲相プロダクトについても簡潔に紹介する。

*気象衛星センターデータ処理部解析課

(2018 年 9 月 6 日受領、2019 年 4 月 12 日受理)